Rayleigh wave phase velocity models for gravitational wave detectors using an array of nodal sensors

Soumen Koley[1*], Henk Jan Bulten[1], Jo van den Brand[1], Maria Bader[1], Xander Campman[2] and Mark Beker[3] study the seismic noise characteristics in the 0.4-8.0 Hz band and uses it for shallow subsurface imaging.

Introduction

Array studies of ambient seismic noise have gained much importance in recent years for the purpose of classifying noise sources corresponding to different frequency bands. Stehly et al. (2006), Snieder et al. (2009), Wapenaar et al. (2010), have also demonstrated useful applications of using ambient noise recordings for surface wave tomography. Seismic motions generated by natural and artificial sources propagate through the subsurface both in the form of body and shear waves. But the major contribution to the seismic noise field is in the form of Rayleigh and Love waves (Haubrich et al., 1963), especially at shallow depths. In the context of gravitational wave detectors, such displacement of the subsurface couples with the suspended elements of the detector through gravitational forces of attraction and is referred to as Newtonian noise. In order to subtract this noise, it is necessary to understand the sources of seismic noise near the detectors and the propagation characteristics. Hence, an optimal seismic array was designed and a passive seismic survey was carried out at the Advanced Virgo gravitational wave detector in Italy. Easily deployable 5 Hz vertical component wireless geophones were used for continuous acquisition of the seismic noise.

Three approaches are of common use for analyzing the direction and velocity of propagation of such seismic noise: the frequency wavenumber (f-k) method (Lacoss et al., 1969), the high resolution frequency wavenumber method (Capon, 1969; Asten and Henstridge, 1984) and the spatial auto-correlation (ESAC) technique (Ohori et al., 2002; Asten et al., 2004). We employ the f-k method for estimating the direction of propagation of different noise sources, and both f-k and ESAC for computing the phase velocities. Seismic noise recorded at Virgo can be categorized into three different frequency bands,

i) Oceanic Microseism 0.2 - 1.0 Hz
ii) Road Bridge Noise 1.5 - 4.0 Hz
iii) Local Noise sources > 4 Hz

The Advanced Virgo gravitational wave detector is located near Pisa, 30 km off the coast of Italy. Hence the micro-seismic energy is mostly dominated by the secondary microseism arising due to coastal reflection and its interaction with the incoming waves. In our study, we focus on the secondary micro-seismic energy observed between 0.2 - 1.0 Hz and aim to quantify only the fundamental mode of Rayleigh wave propagation. Despite the sensitivity limitations of exploration geophones at low frequencies, it was still possible to obtain useful signals down to 0.2 Hz with the high-sensitivity nodal sensors. Beyond 1 Hz, noise originating from local road bridges is observed in the frequency band 1.5 - 4.0 Hz. A dominant peak at 2.5 Hz is observed, especially during working hours of a day. Studies by Acernese et al. (2004) presents a hypothesis that the noise peaked at 2.5 Hz is induced into the ground by oscillations of local road bridges situated approximately 1.5 km away from the interferometer ends. In our analysis we try to verify such predictions, and match our observed noise propagation directions with possible sources in the field. At frequencies above 4.0 Hz sources of noise are mostly local and transient.

Seismic array design

This study makes use of Innoseis Tremornet nodal sensors that allow for rapid deployment and flexible array design, as well as a long recording time on a single battery charge. Designing seismic arrays for studying the phase velocities and direction of propagation of ambient noise pose conflicting restrictions on the selection of inter-sensor spacing. Larger inter-sensor separation helps to increase the resolution of phase velocity estimates for long period waves, while smaller inter-sensor distances prevents the high-frequency waves from getting spatially aliased. Asten and Henstridge (1984) proposed that the maximum sensor separation d_{max} should be at least greater than the maximum wavelength of interest λ_{max} and minimum sensor separation d_{min} must be less than half the minimum wavelength λ_{min}. The second condition follows from the nyquist criterion to avoid spatial aliasing at smaller wavelengths. However, the measure proposed by Woods and Lintz (1973) of using an array response function, is the most widely used method of all. We use this approach for designing an array that is capable of resolving events of frequencies as low as 0.4 Hz, and avoid aliasing up to 8.0 Hz. Given a set of M sensors, with coordinates $[(x_0,y_0), (x_1,y_1) \ldots \ldots (x_{m-1},y_{m-1})]$, the array response vector $a(f)$ can be expressed as,

$$a(f) = \left[e^{-2\pi j \tau_0}, e^{-2\pi j \tau_1}, \ldots, e^{-2\pi j \tau_{m-1}} \right]^T \qquad 2.1$$

[1] National Institute for Subatomic Physics, Nikhef | [2] Shell Global Solutions International B.V. | [3] Innoseis B.V.
* Corresponding author, E-mail: skoley@nikhef.nl

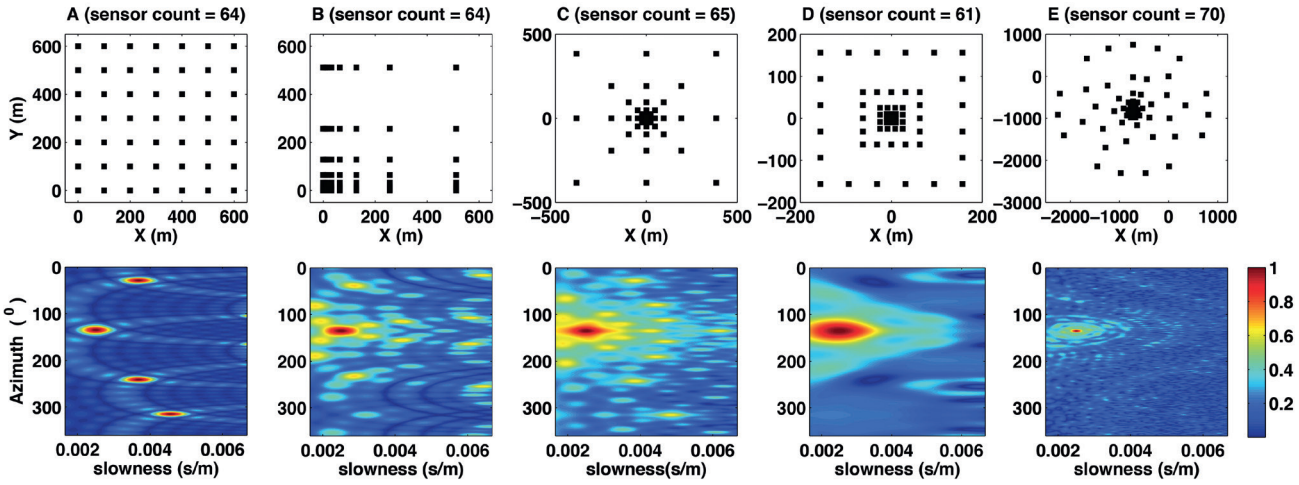

Figure 1. Computed theoretical array response for types of sensor geometries (A, B, C, D and E) at f = 2 Hz, for a plane wave propagating along 135⁰ and velocity of 400 m/s.

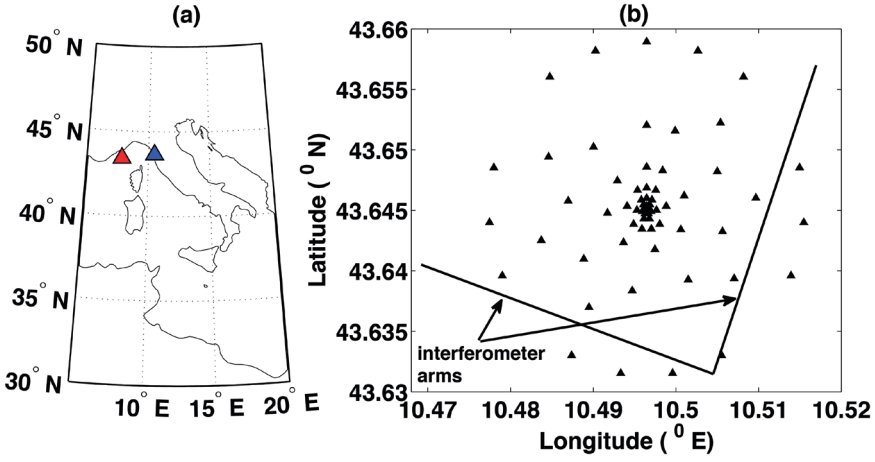

Figure 2 (a) The blue and the red triangle points to the array locations and the Côte d'Azur buoy respectively. (b) Sensor Layout at the Virgo site shown as triangles and the straight lines represent the two 3km-long interferometer arms.

Where, $\tau_m = x_m p\cos\phi + y_m p\sin\phi$ is the time delay for signal to reach the m^{th} sensor from the origin and p, Ø are the slowness and the azimuth of propagation (measured anticlockwise from east). The array response vector corresponding to one particular value of p, Ø is also commonly referred to as the steering vector. Hence, for N_p trial values of slowness and N_ϕ values of azimuth, the total number of steering vectors that can be constructed is $N_p N_\phi$. The array response matrix comprising steering vectors of all possible trial values of slowness and azimuth can be constructed as,

$$A(f) = \left[a_1(f), a_2(f), \ldots, a_{N_p N_\phi}\right] \quad 2.2$$

Using the array response matrix, the theoretical array response corresponding to a plane wave impinging an array along an azimuth $\emptyset_k$ and propagating with slowness p_k is then defined as,

$$AR_k = \frac{1}{N_p N_\phi} A(f) \times a_k^*(f) \quad 2.3$$

The quantity $a_k^*(f)$ represents the complex conjugate of the steering vector. Theoretical array response AR_k attains a value close to unity corresponding to the steering vector that most closely resembles the actual propagation direction, and slowness of the plane wave. All other combinations of the inner product between the steering vector and the columns of the array response matrix contribute to side lobes surrounding the main peak in p – Ø domain. For the passive seismic survey to be carried out at Virgo, the maximum number of sensors that could be used was limited to70.

Figure 1 shows the computed theoretical array response for five different sensor geometries that were tested. Geometry A is a regular spaced grid of 64 sensors with a grid spacing of 100 m. The maximum aperture is 850 m along the diagonals, and a minimum sensor spacing of 100 m. Clearly, the array would suffer from spatial aliasing at higher frequencies because of the too high grid spacing. Spatial aliasing is observed even at 2 Hz for a velocity of propagation of 400 m/s as shown in Figure 1, and hence the design is rejected. Geometry B tries to improve on A by implementing irregular grid spacing. This helps to attain a wide set of interstation distances with minimum grid spacing of 8 m, and maximum of 512 m. The grid spacing is increased in multiples of 2. From Figure 1 we conclude that although such geometry has no aliasing, the side lobe energies are too high and hence can cause problems in source identification if two or more sources are impinging the array simultaneously. The geometry also does not have equal distribution of interstation distances for all azimuths. In order to resolve this issue, geometry C was designed in the form of expanding squares surrounding one cen-

tral sensor. The side of each of the squares was increased again as powers of 2. However, the number of sensors per square was kept constant at 8 and a total of 65 (64 along the squares one in the centre) sensors were used. A minimum sensor separation of 3 m and maximum of 768 m was achieved. Although the array has an azimuthal symmetry, but owing to the same number of sensors in each square, the sensor density was too low for the larger squares. Hence, the side lobe energies are not damped. To resolve this, geometry D was designed that in principle followed the same pattern as C, but the number of sensors in each square was increased by 4 per square. The computed theoretical array response shows no side lobes, and no spatial aliasing. However, the maximum aperture of 560 m would not be large enough for resolving events below 1 Hz. To mitigate all the issues faced so far, a decision was taken to use circular geometries. Geometry E is composed of eight circular rings of radii 6, 12, 24, 48, 96, 192, 768, 1536 m respectively. The number of sensors from the innermost to the outermost ring varied as, 1 (centre), 3, 5, 5, 7, 9, 11, 13, 15. Alternate sensors in the penultimate ring were also shifted by a distance of 100 m, to achieve a better distribution of interstation distances. The array is characterized by a maximum aperture of 3000 m and hence can sample very low frequency events of wavelengths in the same order as the maximum aperture. The array works well for high-frequency events, because of the inner rings of sensors that have a minimum spacing of 6 m. On comparing the theoretical array response of geometry D and E, it is observed that the resolution of array E is far better than D, while ensuring no spatial aliasing. Based on the theoretical array responses computed, geometry E was finalized for deployment at Virgo. Figure 2(a) shows the location of the seismic array by the blue triangle on a map of Italy, and Figure 2(b) shows the array layout on field along with the two 3km-long interferometer arms at Virgo. The array spans the entire Virgo site, and the microseismic energy below 1 Hz would be sampled very well. However, such a large aperture does not guarantee that the plane wavefront assumption will be true for high-frequency events. Hence, for analysing high-frequency events that might originate locally, we propose using only the inner rings of the array up to radius of 200 m. Figure 3(a) shows the distribution of inter-sensor separation and one-way azimuth for all station pairs. The distribution shows a reasonable count for all azimuths and interstation distances.

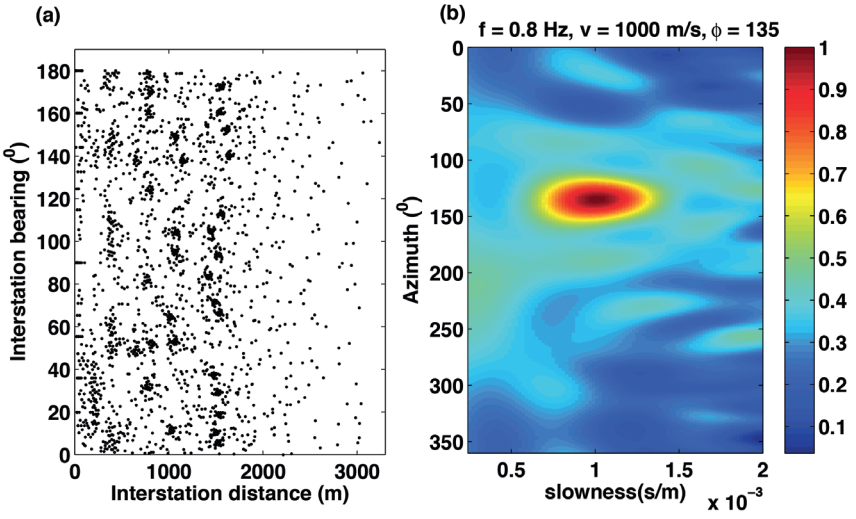

Figure 3 (a) The resulting distribution of distances and one-way azimuths for all interstation paths. (b) Theoretical array response at f = 0.8 Hz for a wave propagating along Ø = 135° and v = 1000 m/s.

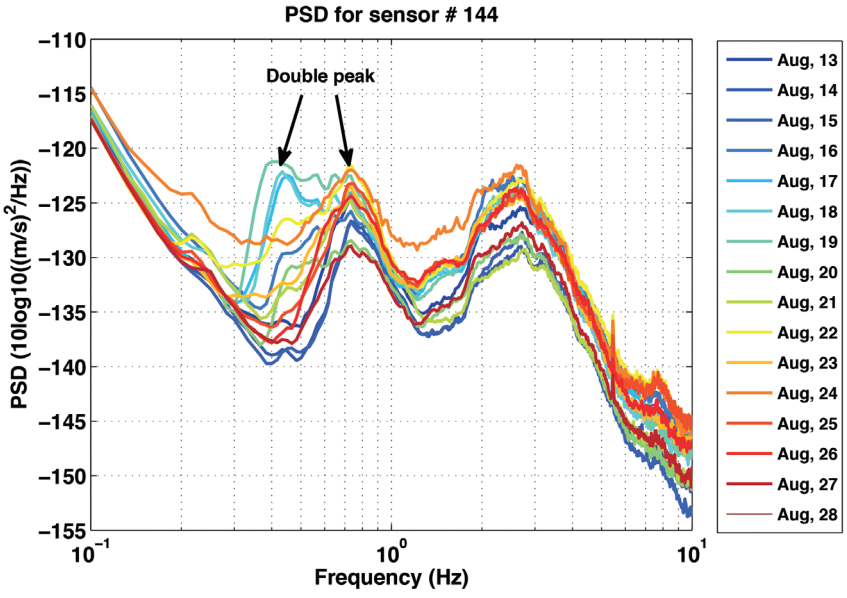

Figure 4 Estimated Power Spectral Density averaged over every day of measurement, from 13 to 28 August, 2016 for station number 0170000144. The arrows shows the presence of double peak in the oceanic microseism.

Figure 3(b) shows the theoretical array response at 0.8 Hz, for a plane wave impinging the array at an azimuth of 135^0, and velocity of 1000 m/s.

Seismic noise sources

Using the designed seismic array, a passive seismic survey was carried out at Virgo for a period of two weeks from 13 August to 28 August, 2016. The oceanic microseism is characterized by a double peak in the frequency band 0.2-1.0 Hz. Figure 4 shows daily averaged power spectral density (PSD) corresponding to 1 of the stations. A peak in the frequency band 0.6-0.8 Hz is observed on all days irrespective of the swell in the Mediterranean Sea. On days when the wave height in the Mediterranean goes above 1 m a secondary peak in the frequency band 0.3-0.5 Hz is also observed. Seismic noise recorded between frequencies 1.5-4.0 Hz is dominated by oscillations induced in the ground by local road bridges. Four road bridges located approximately 1.5-2.0 km from the Virgo interferometer ends were identified to be the sources of noise. Figure 5 shows the location of the road bridges and the interferometer arms. Figure 6(a) and (b) shows the PSD measured beneath one of the bridges and that observed at the Virgo central building. A high correlation is observed in the 1.5-4.0 Hz band. High-frequency oscillations originating at the bridges in the band 5.5-8.0 Hz attenuate by the time it propagates to Virgo. Hence, noise sources at frequencies > 4.0 Hz are mostly local and transient in nature. Noise in the high-frequency band is mostly due to human and local traffic activities. Sharp spectral peaks owing to shaking of building and electric towers were also observed during windy conditions. Figure 7 shows the PSD of the ground motion recorded by a sensor near one of the electric towers and compares it with the wind speed measured by the Virgo anemometer during the time. A significant peak in frequency domain was observed when the wind speed is in excess of 10 km/hr.

Phase velocity and direction of propagation

Beamforming a $f - k$ domain approach is used to estimate the slowness and direction of propagation of the seismic noise. This method first proposed by Lacoss et al. (1969), makes use of the beampower to estimate the steering vector that most closely resembles the actual of direction of propagation and slowness of the seismic noise. The beampower $BP(f)$ at frequency f and corresponding to a steering vector $a_k(f)$ is evaluated as,

$$BP(f) = a_k^*(f) R_{xx}(f) a_k(f) \qquad 3.1$$

$R_{xx}(f)$ is the data covariance matrix in frequency domain, and $a_k^*(f)$ represents the complex conjugate of the steering vector corresponding to the k^{th} combination of p, Ø. The combination of p, Ø corresponding to the maximum value of beampower gives an estimate of the propagation direction and slowness at frequency f. For the oceanic microseism, beampower is computed for every hour of data and the data covariance matrix $R_{xx}(f)$ is evaluated by further subdividing every hour of data into 12 windows. For a network of 64 sensors, the data matrix $R(f)$ is of the form 64 × 12 matrix, and $R_{xx}(f)$ is computed as $X(f)X^*(f)$. Hence, the

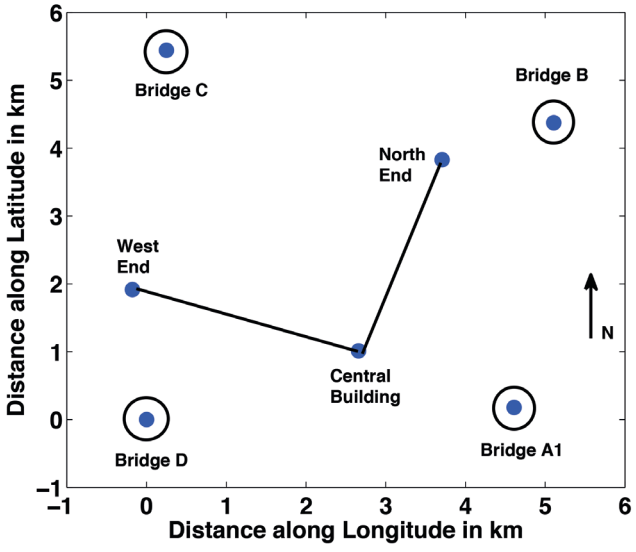

Figure 5 Location of the four road bridges A1, B, C and D near Virgo.

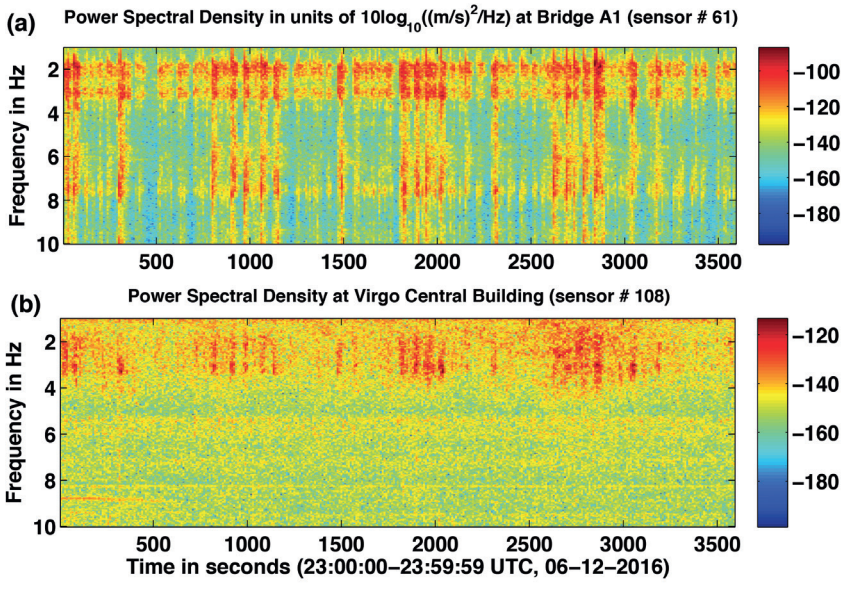

Figure 6 (a) PSD of the ground motion observed beneath bridge A1, situated 1.5 km south east of Virgo central building. (b) PSD of the ground motion observed at the Virgo central building during the same time.

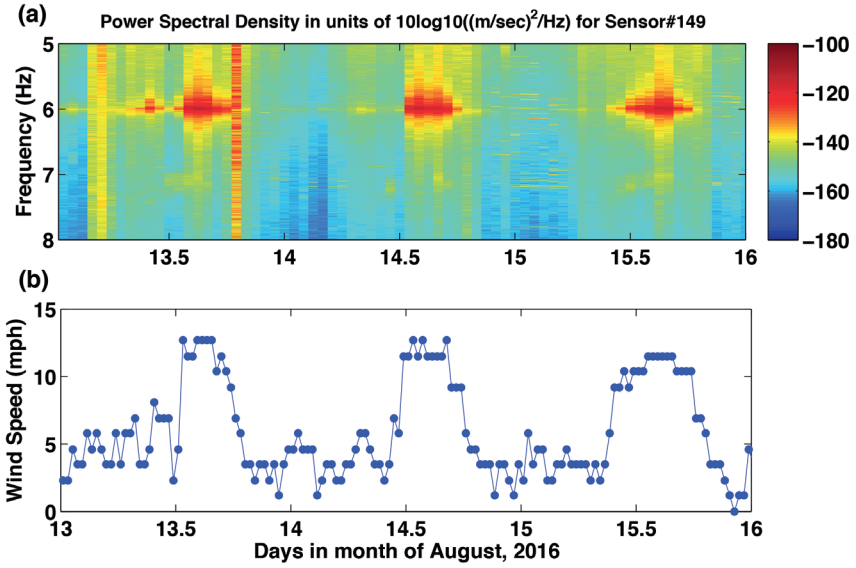

Figure 7 (a) PSD of the ground motion recorded near an electric tower. (b) Wind speeds recorded at Virgo during the same period.

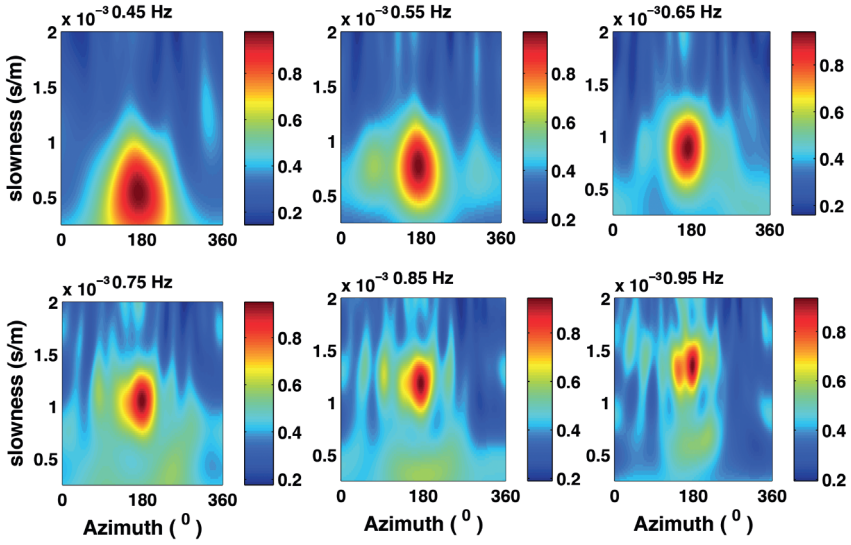

Figure 8 Beamforming output showing normalized beampower as a function of slowness and azimuth for 18 August, 2016 at frequencies between 0.45-0.95 Hz.

beampower is estimated as a function of *p*, Ø, *f* and time *t*. We represent the results in two types of plots. First we fix the time window and the frequency, and express the beampower only as a function of *p*, Ø. Figure 8 is an example of such a representation. The beampower is plotted as a surface in *p* – Ø domain for a day's measurement, at discrete frequencies. Secondly, we express the beampower as a function of azimuth of propagation and time for a given frequency. The beampower is initially stacked for all values of slowness and expressed only as a function of azimuth for a given time window and frequency. The process is then repeated for several time windows and the beampower is plotted as a surface, where the azimuth is measured anti-clockwise from the x-axis and the time is plotted radially outwards. This plot gives us an idea about the change in the estimated propagation direction as a function of time. Figure 9 shows such a plot for six days of measurements. The radial axis in all the plots in Figure 9 represents time in hours and azimuth is measured anti-clockwise from the x-axis. Propagation velocities range between 2 and 1.2 km/s, as can be seen from Figure 8. Propagation azimuth for the oceanic microseism was observed to be close to 180^0 and can be attributed to the waves from the Mediterranean Sea hitting the coast at Pisa.

Beamforming is also used for estimating the direction of propagation of road bridge noise. Beamforming is performed on smaller time segments because of the multiple sources of noise in this frequency band. The data matrix $X(f)$ is computed for every 300 s of data at a time. Each stretch of 300 s is further subdivided into five segments of 60 s each, and the data matrix takes the form of a 64 x 5 matrix. Figure 10 shows the beampower as a function of azimuth and time, for six days of measurement. The arrows in the figure show the directions along which the road bridges are located. Dominant noise was seen to originate from the bridges at azimuth of and. Road Bridge C near the north end of the interferometer was also observed to contribute to the measured noise on a few days. Figure 11a and 11b shows Rayleigh wave phase velocity corresponding to the oceanic microseism and the road bridge noise respectively. Noise originating owing to the road bridges in the frequency band 1.5-4.0 Hz propagates with velocities in the range 450-150 m/s. Owing to the circular geometry of the seismic array it was possible to estimate the phase velocities

at higher frequencies using ESAC. Only the inner six rings extending up to a radius of 192 m was used for the analysis and phase velocities were estimated in the 2.0-8.0 Hz frequency band. Figure 12 shows the Rayleigh wave phase velocity dispersion curve estimated using Beamforming and ESAC.

Dispersion curve inversion

The Rayleigh wave phase velocity dispersion curve is inverted to obtain a one dimensional S-wave velocity model for the region. The parameter space for the inversion includes the P-wave velocity, S-wave velocity, density and depth of each layer. Given that a subsurface model is known, it is possible to compute a dispersion curve pertaining to the model. The forward problem of computing theoretical dispersion curves is accomplished using the Thomson-Haskell propagator matrix method (Haskell, 1953). In order to obtain the best subsurface model, an inversion is carried out using the neigbourhood algorithm as proposed by Sambridge (1999). The solution to such an inverse problem is non-unique, and highly ill-posed with respect to the P-wave velocity and density of the subsurface model. Hence, a priori information about the subsurface must be incorporated in the inverse problem.

Virgo is located on the southern basin of river Arno, which is characterized by marine and continental deposits over Mesozoic bedrock, formed mainly during the Middle Miocene period (Patacca et al., 1990). A set of north-west striking normal faults

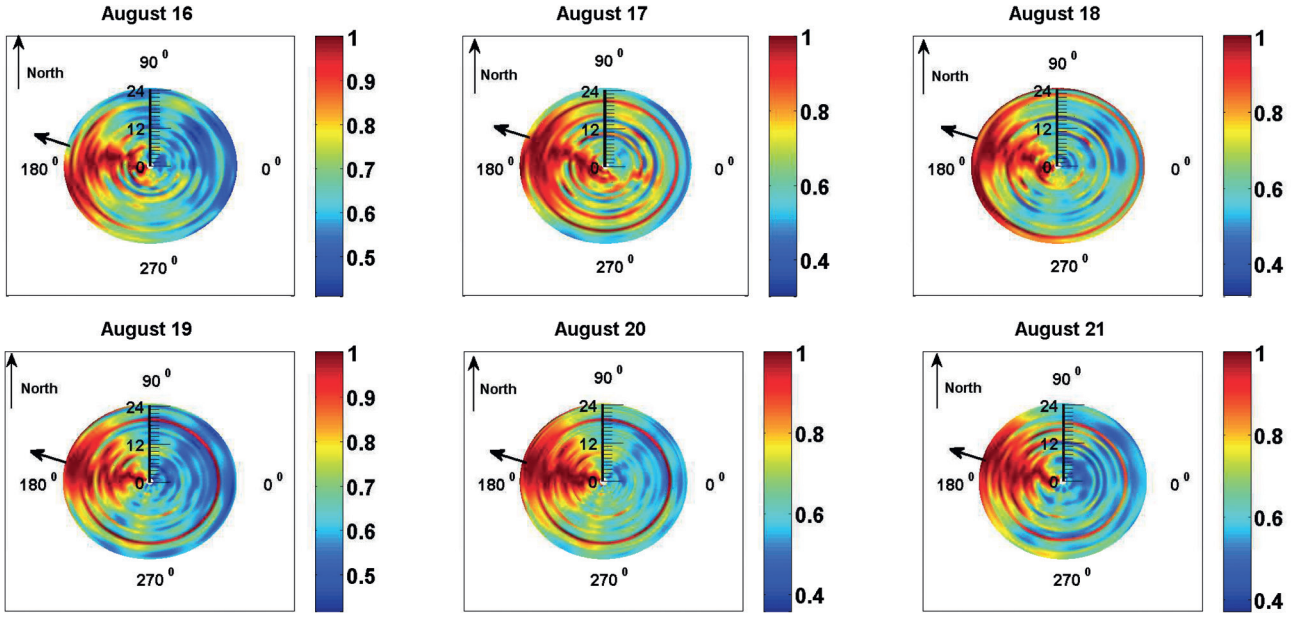

Figure 9 Beamforming output showing normalized beampower as a function of time and azimuth for 16-21 August, 2016 at f = 0.65 Hz. On the radial axis is time (1-24 hours) and the azimuth is measured anticlockwise from east. The arrow points to the direction of the Mediterranean Sea.

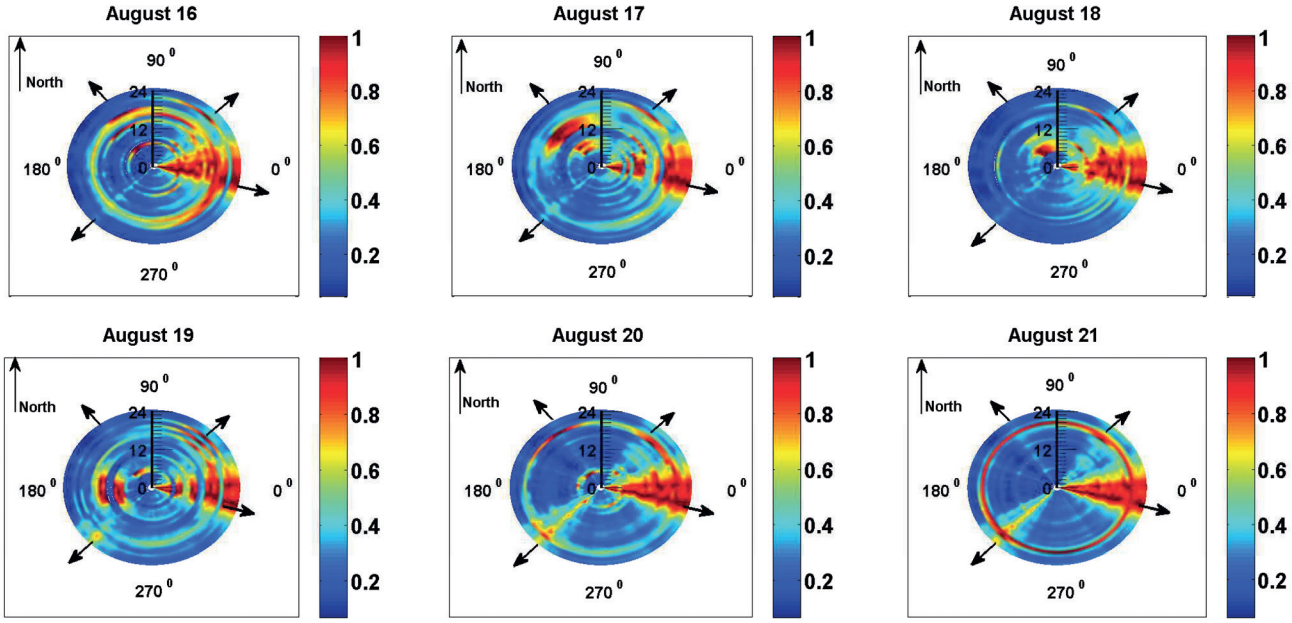

Figure 10 Beamforming output showing normalized beampower as a function of time and azimuth for 16-21 August, 2016 at f = 2.5 Hz. On the radial axis is time (1-24 hours) and the azimuth is measured anticlockwise from east. The arrow points to the location of the road bridges near the Virgo site.

Formation Type	Vp search range (m/s)	Vs search range (m/s)	Density search range (kg/m³)	Layer depth (m)	Poisson's ratio
Mud and Clay	150 - 250	75 - 140	1700	0 – 5	0.2 - 0.5
Sand	200 - 350	100 - 160	1800	5 – 10	0.2 - 0.5
Sand and Clay	200 - 350	120 - 180	1800	10 – 15	0.2 - 0.5
Sand	350 - 500	150 - 250	1900	15 – 25	0.2 - 0.5
Gravel	400 - 700	150 - 300	1900	25 – 40	0.2 - 0.5
Organic Clay	600 - 1200	150 - 400	1900 - 2100	40 – 80	0.2 - 0.5
Pliocenic deposits	1200 - 2000	300 - 800	2100 - 2500	100 – 250	0.2 - 0.5
Carbonate formation	1500 - 3000	500 - 1500	2300 - 2600	600 – 800	0.2 - 0.5
Half space	2000 - 4000	1000 - 3500	2600 - 2700		0.2 - 0.5

Table 1 Summary of the parameter space explored by the inversion algorithm for obtaining the best fit subsurface model.

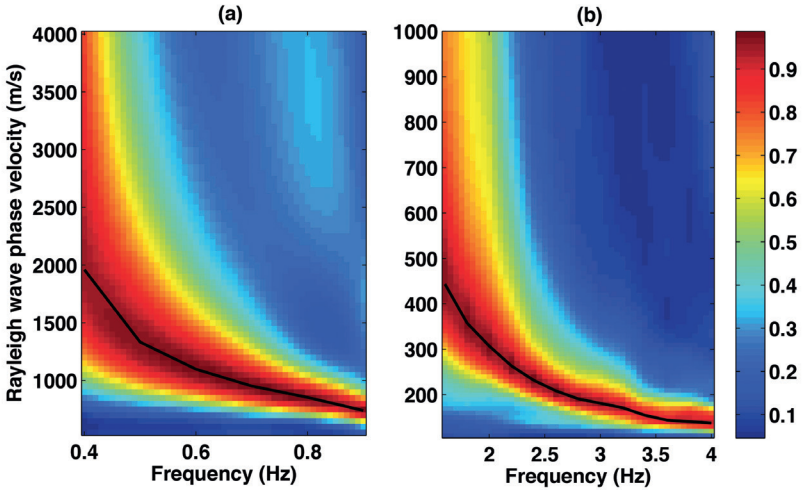

Figure 11 Rayleigh wave phase velocity dispersion curve estimated using beamforming corresponding to the (a) Oceanic Microseism 0.4-1.0 Hz and (b) Road Bridge noise 1.5-4.0 Hz.

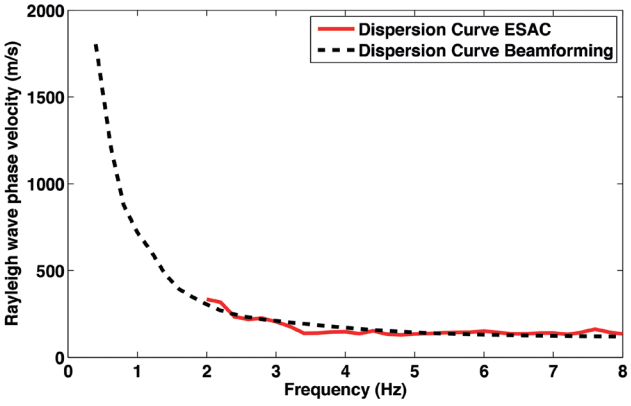

Figure 12 Rayleigh wave phase velocity dispersion curve obtained using beamforming (0.4-8.0 Hz) and ESAC (2.0-8.0 Hz).

also span the basin. Hence as one goes from E-W a dipping carbonate bedrock formation that stretches from 700 m deep in the eastern end, to 2500 m deep or more to the west end is present (Cantini et al., 2001). Shallow subsurface geology up to 70 m is well studied through boreholes, and gravimetric studies (Stefanelli et al., 2008). According to these studies the upper 70 m of subsurface is formed mainly because of glacial activity and eustatic changes during Pleistocene period. The top layer of the subsurface at Virgo is formed of mud and clay of density 1500 kg/m³ and extends up to a depth of 25 m. This is followed by a thin layer of sand, and conglomerates of density 1700 and 2100 kg/m³ respectively. The last layer, as evident from gravimetric studies, is of organic clay and mud with a density of 1800 kg/m³. Multichannel Analysis of Surface Waves (MASW) using linear 1D arrays have also been carried out at Virgo in 2013. Based on these studies we further subdivide the top 25 m of the subsurface into more layers. The parameter space over which a search is performed for estimating the best P-wave, S-wave, density and depth of each layer of the subsurface is shown in Table 1. Since the values of density were known deterministically from micro-gravity gradient studies, they were fixed to a depth of 70 m. The inversion is also carried out for a nine layer model and a total of 60,000 models were explored. A minimum relative misfit value of 0.018 was achieved. Figure 13 (a) and (b) shows all the S-wave velocity models explored and their corresponding theoretical dispersion curves, with the relative misfit values of each model shown in the colourbar. The velocity model in red in Figure 13a shows the best fit model, and the estimated dispersion curve matches well with the observed dispersion curve (black) as shown in Figure 13b. Figure 13c shows a comparison of the velocity model obtained from this study, and compares with the estimated models from previous MASW studies.

Conclusion

In this paper, we have demonstrated the use of surface wave methods for estimating the phase velocity and direction of propagation

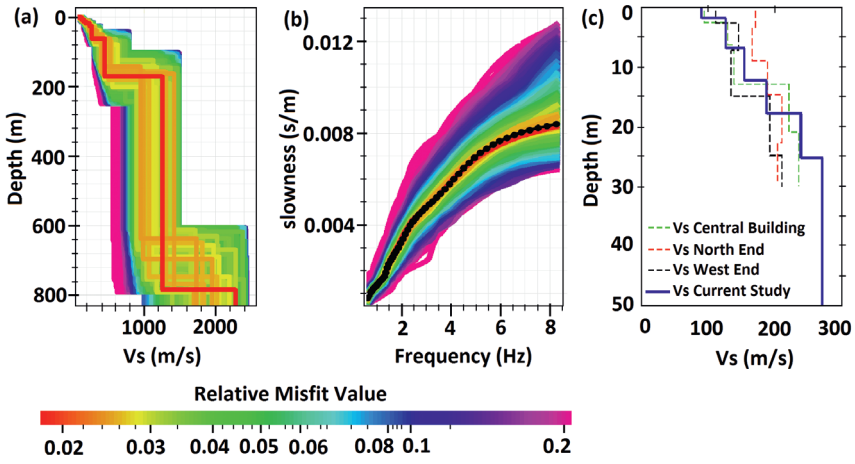

Figure 13 (a) S-wave velocity models explored for a nine-layer model, with red line showing the best model having minimum misfit. (b) Theoretical dispersion curves corresponding to all explored models in (a) and the measured dispersion curve shown in black. (c) V_s model from this study and previous MASW measurements for top 50 m.

of ambient seismic noise. Using the measured Rayleigh wave phase velocities, an inversion was carried out to obtain a 1D S-wave velocity model in the region. MASW studies generally rely on the use of hammer or weight dropper for generating surface waves that are further used to investigate the subsurface properties. However, in this study we aimed to use the ambient seismic noise like the oceanic microseism and the road bridge noise. The use of wireless sensors significantly contributed to designing a seismic array that could sample the seismic noise over a broad frequency range. The passive seismic survey conducted was aimed at obtaining a preliminary idea of the seismic noise sources and its propagation. In future, we plan to deploy more sensors targeting the specific noise sources that were deciphered from this survey. Future plans also include designing algorithms that would facilitate accurate computation of the Newtonian noise associated with these sources and then subtracting it from the interferometer measurements.

References

Acernese, F., Amico P., Arnaud N., Babusci D., Barillé R., Barone F., Barsotti L., Barsuglia M., Beauville F. and Bizouard M., et al. [2004]. Properties of seismic noise at the Virgo site. *Classical and Quantum Gravity*, **21**, S433.

Acernese, F., Antonucci F., Aoudia S., Arun K., Astone P., Ballardin G., Barone F., Barsuglia M., Bauer T.S. and Beker M., et al. [2010]. Measurements of superattenuator seismic isolation by Virgo interferometer. *Astroparticle Physics*, **33**, 182–189.

Asten, M. and Henstridge J. [1984]. Array estimators and the use of microseisms for reconnaissance of sedimentary basins. *Geophysics*, **49**, 1828–1837.

Asten, M. W., Dhu T. and Lam N. [2004]. Optimized array design for microtremor array studies applied to site classification; comparison of results with scpt logs. *Proceedings of the 13th World Conference on Earthquake Engineering*, Abstracts.

Cantini, P., Testa G., Zanchetta G. and Cavallini R. [2001]. The Plio–Pleistocene evolution of extensional tectonics in northern Tuscany, as constrained by new gravimetric data from the Montecarlo basin (lower Arno Valley, Italy). *Tectonophysics*, **330**, 25–43.

Capon, J. [1969]. High-resolution frequency-wavenumber spectrum analysis. *Proceedings of the IEEE*, **57**, 1408–1418.

Haskell, N. A. [1953]. The dispersion of surface waves on multilayered media. *Bulletin of the Seismological Society of America*, **43**, 17–34.

Haubrich, R., Munk W. and Snodgrass F. [1963]. Comparative spectra of microseisms and swell. *Bulletin of the Seismological Society of America*, **53**, 27–37.

Hughes, S. A. and Thorne K.S. [1998]. Seismic gravity-gradient noise in interferometric gravitational-wave detectors. *Physical Review D*, **58**, 122002.

Lacoss, R.T., Kelly E.J. and M.N. Toksöz [1969]. Estimation of seismic noise structure using arrays. *Geophysics*, **34**, 21–38.

Ohori, M., Nobata A. and Wakamatsu K. [2002]. A comparison of ESAC and FK methods of estimating phase velocity using arbitrarily shaped microtremor arrays. *Bulletin of the Seismological Society of America*, **92**, 2323–2332.

Patacca, E., Sartori R. and Scandone P. [1990]. Tyrrhenian basin and Apenninic arcs: kinematic relations since late Tortonian times. *Mem. Soc. Geol. It,* **45**, 425–451.

Sambridge, M. [1999]. Geophysical inversion with a neighborhood algorithm-II. Appraising the ensemble. *Geophysical Journal International*, **138**, 727–746.

Saulson, P.R. [1994]. Fundamentals of interferometric gravitational wave detectors. World Scientific.

Snieder, R., Miyazawa M., Slob E., Vasconcelos I. and Wapenaar K. [2009]. A comparison of strategies for seismic interferometry. *Surveys in Geophysics*, **30**, 503–523.

Stefanelli, P., Carmisciano C., Caratori Tontini F., Cocchi L., Beverini N., Fidecaro F. and Embriaco D. [2008]. Microgravity vertical gradient measurement in the site of VIRGO interferometric antenna (Pisa plain, Italy). *Annals of Geophysics*, **51**, 877-886.

Stehly, L., Campillo M. and Shapiro N. [2006]. A study of the seismic noise from its long-range correlation properties. *Journal of Geophysical Research: Solid Earth*, 111, B10306.

Wapenaar, K., Draganov D., Snieder R., Campman X. and Verdel A. [2010]. Tutorial on seismic interferometry: Part 1 basic principles and applications. *Geophysics*, **75**, 75A195–75A209.

Wathelet, M., Jongmans D. and Ohrnberger M. [2004]. Surface-wave inversion using a direct search algorithm and its application to ambient vibration measurements. *Near Surface Geophysics*, **2**, 211–221.

Woods, J. W., and Lintz P.R. [1973]. Plane waves at small arrays. *Geophysics*, **38**, 1023–1041.

INTERPRETING BELOW SEISMIC TUNING WAS A TOUGH NUT TO CRACK...

PARADISE
Multi-Attribute Analysis
lives here

DISCOVER HOW WE DID IT.

EAGE 2017 | BOOTH 350

GEOPHYSICAL INSIGHTS
FROM INSIGHT TO FORESIGHT

Hear Industry Thought Leaders

Profile of the Future Interpreter

DR. KURT MARFURT
Principal Investigator of the AASPI Consortium at The University of Oklahoma

Seismic Interpretation Below Tuning with Multi-Attribute Analysis

ROCKY RODEN
Geophysical Insights
Sr. Consulting Geophysicist

An Introduction to the World of Attributes: Applications and Case

DR. CHINGWEN CHEN
Geophysical Insights
Sr. Geophysicist

Finding Oil & Gas Using Multi-Attribute Analysis

DEBORAH SACREY
Geophysical Insights
Sr. Geoscientist

Paradise – The Road Ahead

MICHAEL DUNN
Geophysical Insights
Sr. VP – Business Development

An Introduction to Multi-Attribute Analysis – Tour Paradise

HAL GREEN
Geophysical Insights
Director – Marketing/BD

www.geoinsights.com

FracGeo
The Future of Shale Management, Today

One Day, One Software, One Training
For Engineers and Geoscientists

Surface drilling data for geomechanical properties
Petrophysics for unconventional reservoirs
Seismic inversions and attributes
Complex structural frameworks and 3D grids
Constrained 3D geologic and natural fracture models
Well performance predictions using AI & Data Analytics
Reservoir geomechanics validated with microseismicity
Constrained frac design and proppant distribution
Constrained reservoir simulation and pressure depletion
Economics

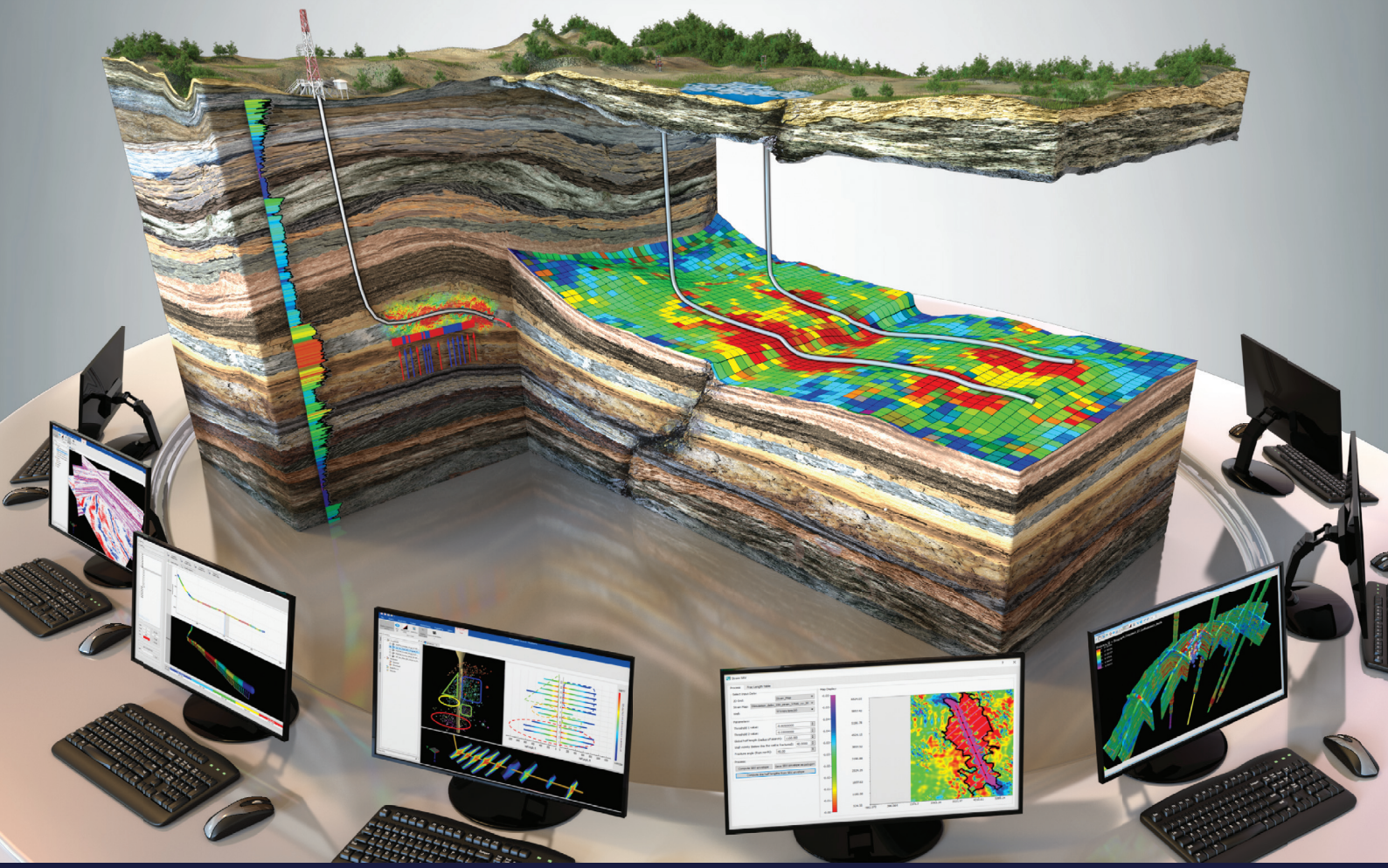

Are unconSTRAINed reservoir models STRESSing you out?

Register for training in Paris June 9 and June 16 to learn new 3G techniques to reduce uncertainty in your geologic and natural fracture models, and geomechanically constrain frac design and reservoir simulation

FracPredictor™
The First and Only 3G Integrated Software Platform


DrillPredictor™

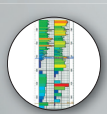
LogPredictor™

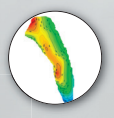
MapPredictor™

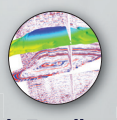
SeisPredictor™


StratPredictor™


RockPredictor™

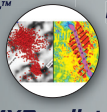
GMXPredictor™

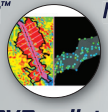
SRVPredictor™


StimPredictor™

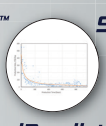
ProdPredictor™


EconPredictor™

www.FracGeo.com/training

Powered by GEO Engineering Magma™ SDK